CHAPTER 3

Hybrid Perovskite $CH_3NH_3PbI_3$/ZnO Heterostructure Based High Performance Photodetectors

3.1 Introduction

We have already discussed in Chapter-1 that the hybrid perovskite materials have drawn considerable interest of the researchers for optoelectronic applications due to their high photoabsorption coefficients, optimum bandgap properties, high charge carrier mobilities, good solubility, long carrier lifetimes and solution processing based low fabrication cost [33], [36]. These materials show efficient photo absorbing characteristics in the visible spectrum [61]. The interface layers such as the electron transport layer (ETL) and hole transport layer (HTL) are often required for improving the stability of the hybrid perovskites as well as for the performance enhancement of the hybrid perovskite-based devices [127], [128]. The hybrid perovskite-based photodetectors have shown high responsivity over a wide detection range. It is discussed in Chapter-1 that wide bandgap n-type materials like ZnO, TiO_2, SnO_2, etc. are generally used for ETL and p-type materials like PEDOT: PSS, Spiro-OMETAD, P3HT, MoOx, NiOx, etc. are commonly used for the HTL in the hybrid perovskite-based p-i-n structured photodetector [43]-[44], [47]-[48], [129]-[131]. Gao *et al.* [132] have fabricated a $CH_3NH_3PbI_3$/ZnO based horizontal photodetector to achieve the responsivity of 4 A/W at 380 nm. Xue *et al.* [133] have reported a $CH_3NH_3PbI_3$/ZnO based vertical heterostructure using spiro-OMeTAD as HTL material to achieve the responsivity of 7.8 A/W at 365 nm. It shows that HTL material plays a significant role in the performance improvement of the hybrid perovskite $CH_3NH_3PbI_3$ based photodetectors. Thus, after investigating the performance

characteristics of $BiFeO_3$/ZnO heterojunction for white light detection, the present chapter considers the performance investigation of a heterojunction device formed between the most widely used hybrid perovskite $CH_3NH_3PbI_3$ and ZnO for photodetection applications. In this work, a vertical $CH_3NH_3PbI_3$/ZnO heterostructure photodetector device is fabricated using a low-cost solution processing method using MoOx for the HTL material. The ZnO layer acts as a UV light absorber as well as the ETL of the device. The layout of the present chapter is given in the following.

Section 3.2 presents the experimental details of the fabrication of the hybrid perovskite $CH_3NH_3PbI_3$/ZnO heterostructure based photodetector device under study. The results and discussion related to the thin film characterizations and photoresponse measurements of the proposed device are presented in section 3.3. Finally, section 3.4 is used to conclude the chapter.

3.1 Experimental Details

3.1.1 Materials Synthesis

All the chemicals are used as received from Sigma-Aldrich and Merck Chemicals without any further purifications. The ZnO NPs were synthesized by the sol-gel route. Zinc acetate dihydrate [Zn $(CH_3CO_2)_2 \cdot 2H_2O$] precursor was mixed with a solvent of an equal molar ratio of monoethanolamine (MEA) and 2-methoxy ethanol in ambient condition. Initially, 1 M (2.1949 gm) zinc acetate [Zn $(CH_3CO_2)_2 \cdot 2H_2O$] was dissolved in 2-methoxy ethanol (10 ml) and stirred the solution continuously for more than 2 hours on a hot plate to gradually increase its temperature up to a fixed temperature of 60°C. MEA (reagent) (1.2 ml) was then quickly injected into the stirred solution at 60°C for growing colloidal ZnO NPs [118]. A schematic representation of the synthesis of the ZnO NPs is shown in Figure 3.1.

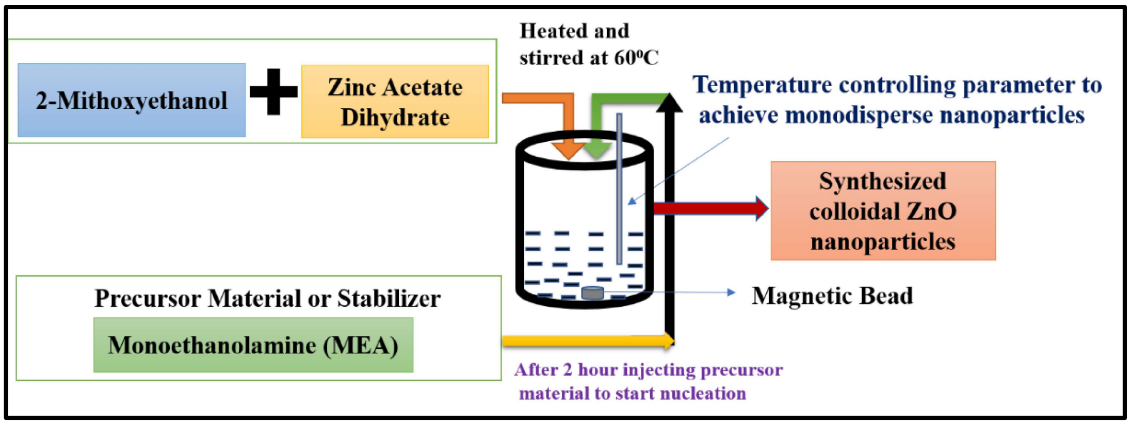

Figure 3.1: Synthesis of the ZnO nanoparticles.

The hybrid perovskite $CH_3NH_3PbI_3$ is also synthesized by a sol-gel route. A precursor solution of hybrid $CH_3NH_3PbI_3$ was composed using an equimolar (1:1) mixture of (0.15897 gm) methylammonium iodide (CH_3NH_3I) and of (0.46101 gm) lead iodide (PbI_2) [43], [44]. The solvent of (CH_3NH_3I) and lead iodide (PbI_2) solution was (1 ml each) N, N-dimethylformamide anhydrous (DMF) and put this solution for stirring at room temperature for 24 hours. Finally, the yellowish colour solution of hybrid perovskite $CH_3NH_3PbI_3$ is obtained. A schematic representation of the synthesis of the hybrid perovskite $CH_3NH_3PbI_3$ nanoparticles is shown in Figure 3.2.

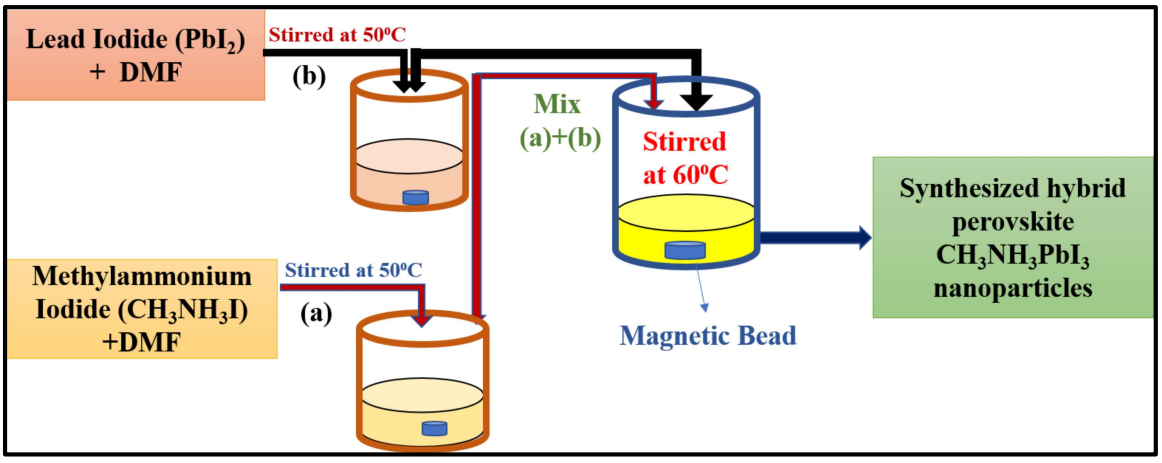

Figure 3.2: Synthesis of the hybrid perovskite $CH_3NH_3PbI_3$ nanoparticles.

3.2.2 Device Fabrication

In this section, we are discussing the substrate cleaning process, thin-film deposition in detail.

3.2.2.1 Substrate Cleaning

In the present work fluorine-doped tin oxide (FTO) glass substrates with thickness, ~2.2 mm and resistivity ~7-10 (ohm.cm) was cut into small regular square-shaped (15×15 mm^2) using a diamond cutter. The small FTO substrate piece was cleaned thoroughly. At first, FTO coated glass substrates were sequentially cleaned in an ultrasonic cleaning bath in a 5% soap solution to remove dust particles for 15 min., then deionized (DI) water with a resistivity of ~18 (MΩ.cm) to get rid of chemical residues for 15 min., then acetone (C_3H_6O) to remove the organic remnants/contaminants from the substrate for 15 min., at last, cleaned by isopropanol (C_3H_8O) for 10 minutes to remove organic residues left on substrate. Then, the substrates were treated by plasma cleaning in the presence of oxygen and argon for 20 minutes to increase the hydrophilicity of FTO coated glass substrate.

3.2.2.2 Thin Film Deposition

In the first deposition step, ZnO NPs dispersed solution was deposited on the as cleaned FTO coated glass substrate by the spin coating unit (TSE, Model SPM-150LC, Germany) at 2000 rpm for 30 s. The process was optimized and repeated two times (at same speed and duration) to obtain a ZnO NPs layer thickness of ~120 nm. Then ZnO NPs coated FTO samples were annealed at 450^0C for 2 hours in a muffle furnace. In the second step, the hybrid perovskite $CH_3NH_3PbI_3$ NPs solution was used to grow a thin layer of $CH_3NH_3PbI_3$ NPs on the ZnO NPs layer using the spin coating method at 2000 rpm for 40 s. The process is repeated three times to obtain the thickness of ~250 nm and

each time the film is dried at 80°C for 10 minutes. Finally, the hybrid perovskite $CH_3NH_3PbI_3$ thin film is annealed at 110°C on a hot plate for 30 minutes under ambient conditions. In the third step, the MoOx thin film of ~12 nm is deposited by using the thermal evaporation unit (Model No. FL400, SMART COAT 3.0 A, Hind High Vacuum India). The MoOx powder was heated in the muffle furnace at 100°C for 30 minutes. Then thoroughly cleaned substrate was placed in thermal beam chamber and source material (MoOx powder) was kept in the thermal evaporation unit at a vacuum of ~10^{-6} mbar with a deposition rate of ~0.03 Å/s inside the thermal evaporation unit. For contact electrode formation, Ag (99.99%) metal dots of ~2 mm diameter (device area 0.0314 cm^2) and ~100 nm thickness were fabricated on the MoOx layer by thermal evaporation unit (Model No. FL400, SMART COAT 3.0 A, Hind High Vacuum India) with the shadow mask technique. The vacuum level was maintained in the range of 10^{-6} mbar with a deposition rate of 0.02 Å/s in the thermal evaporation unit. The thicknesses of different layers of the device were measured using the optical spectrometer commonly known as F20-UV, thin-film analyzer (Model No. SDT2, Filmetrics USA) instrument. A schematic representation of the fabricated steps used for the fabrication of hybrid perovskite $CH_3NH_3PbI_3$ based photodetector is shown in Figure 3.3.

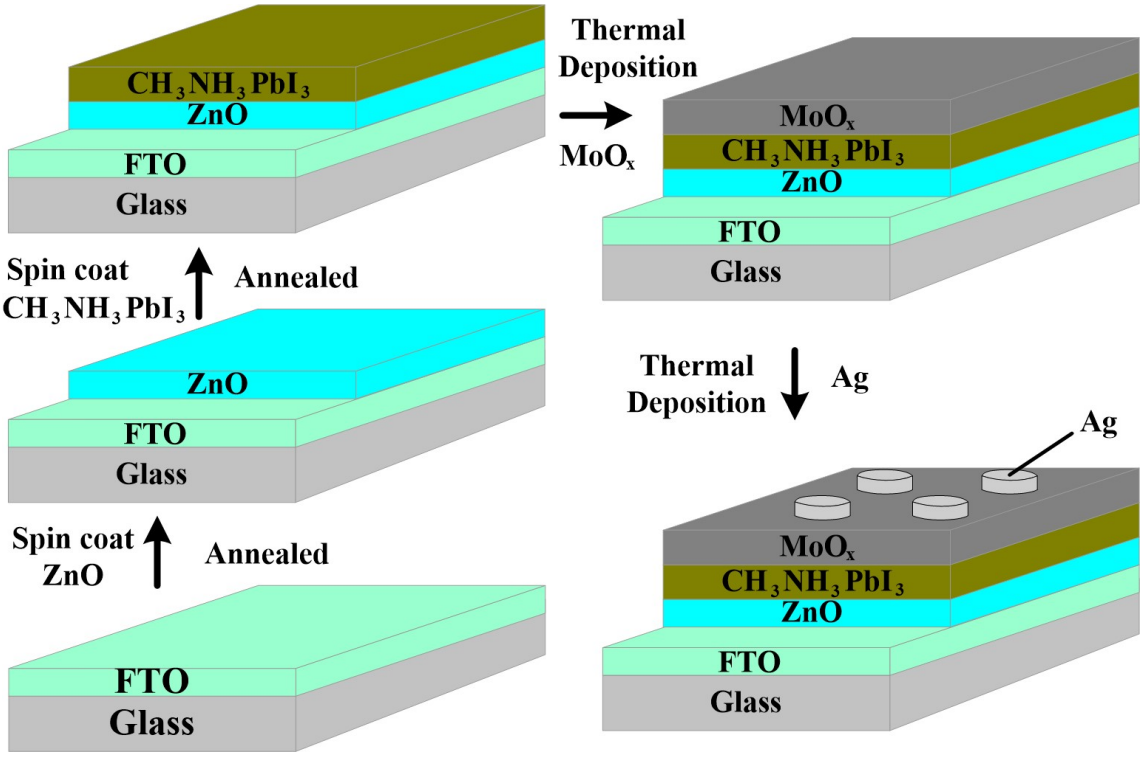

Figure 3.3: Schematic representation of the fabricated steps used for fabrication of hybrid perovskite $CH_3NH_3PbI_3$ based photodetector device.

3.3 Results and Discussion

In this section, structural, optical and electrical characterization of hybrid perovskite $CH_3NH_3PbI_3$/ZnO heterostructure device, are performed.

3.3.1 Thin Film Characterizations

(a) Crystallographic orientation by XRD Analysis

The crystalline structure of ZnO thin film and hybrid perovskite $CH_3NH_3PbI_3$ nanoparticles have been investigated by X-ray diffraction (RIGAKU-Smart XDMAX, PC-20, 18-Kw Cu rotating anode, Rigaku, Tokyo) at room temperature. The obtained XRD spectra of ZnO NPs has been shown in Figure 3.4. The diffraction peaks found in the XRD spectra of ZnO NPs at 31.2°, 33.9°, 35.8°, 47.1° and 56.1° are assigned to the diffractions from the (100), (002), (101), (102) and (110) planes, respectively. The obtained diffraction peaks are well matched to the hexagonal wurtzite structure of ZnO

(JCPDS card No. 36-1451, a = 0.325 nm and c =0.521 nm) without any contaminations and high purity [119], [120]. The thin film of $CH_3NH_3PbI_3$ is investigated using XRD in continuous scan mode from XRD angle (2θ, 10 degrees to 60 degrees). The obtained XRD spectra of $CH_3NH_3PbI_3$ NPs has been shown in Figure 3.5. The preferred orientations at 14.48°, 28.93°, 32.20°, 40.86°, 43.51° are observed, with these assigned to the (110), (220), (310), (224) and (330) planes, respectively of $CH_3NH_3PbI_3$ perovskite tetragonal structure and orientations at 20.06°, 24.05°, 24.64°, 35.50°, 51.25°and 52.60° assigned to the minor facet (200), (211), (202), (312), (404), (226) planes, respectively, which indicated that perovskite film is of high phase purity [132].

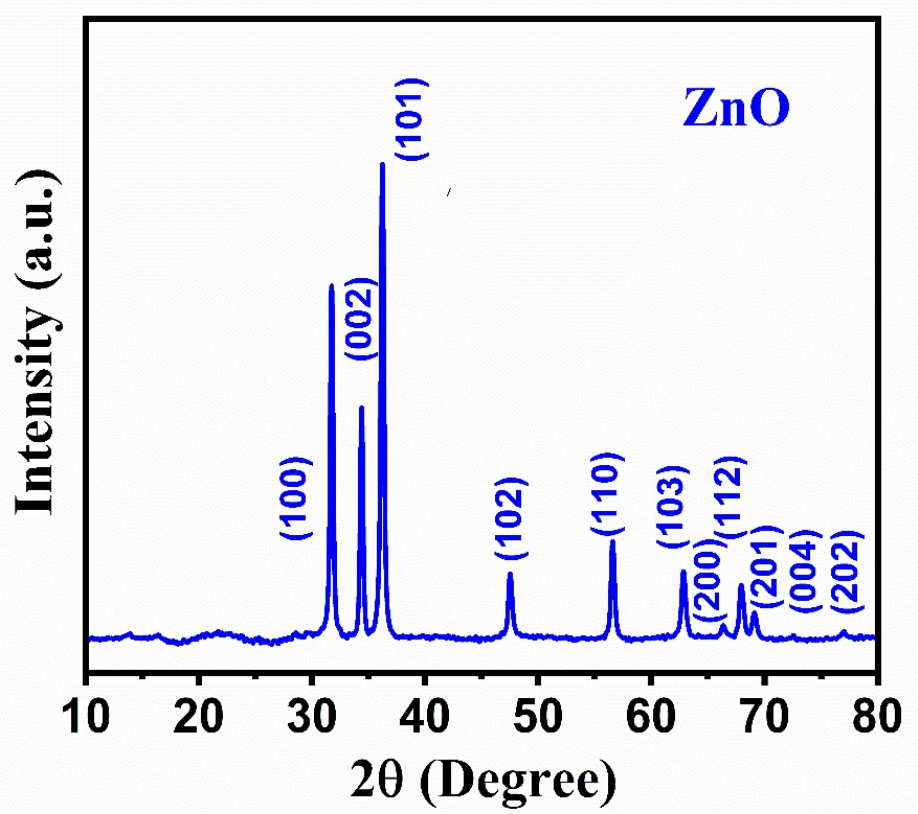

Figure 3.4: XRD peaks of the ZnO NPs thin film deposited on the glass substrate using X-ray diffraction (RIGAKU-Smart XDMAX, PC-20, 18-Kw Cu rotating anode, Rigaku, Tokyo) at room temperature.

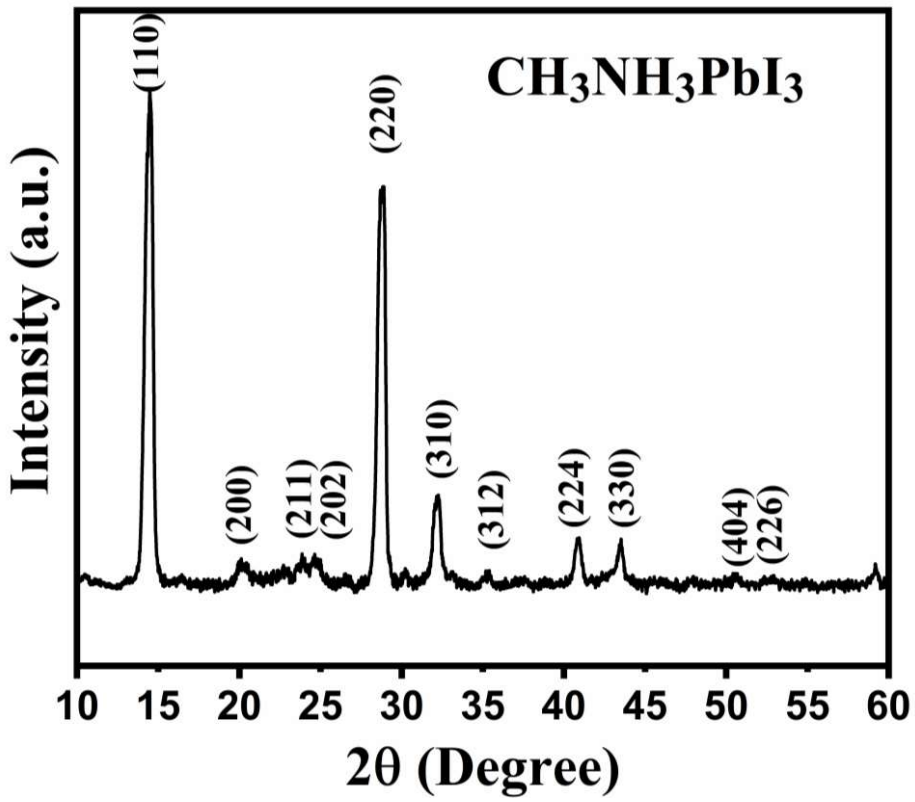

Figure 3.5: XRD pattern of the perovskite $CH_3NH_3PbI_3$ thin film deposited on the glass substrate using X-ray diffraction (RIGAKU-Smart XDMAX, PC-20, 18-Kw Cu rotating anode, Rigaku, Tokyo) at room temperature.

(b) Surface Morphology

The surface morphology of the synthesized ZnO NPs and hybrid perovskite $CH_3NH_3PbI_3$ NPs are investigated using a high-resolution scanning electron microscope (HRSEM, Nova Nano SEM 450, USA). HRSEM image of ZnO thin film after annealing at 450^0C for 2 hours is shown in Figure 3.6. The ZnO thin film has uniformly grown nanoparticles in the range of 20-40 nm in diameter with high density. HRSEM image of perovskite $CH_3NH_3PbI_3$ thin film after annealing at 110^0C for 30 mins is shown in Figure 3.7. The $CH_3NH_3PbI_3$ film has uniformly grown nanoparticles in the range of 50-100 nm in diameter with high density. Small particle sizes of ZnO and perovskite $CH_3NH_3PbI_3$ thin films enhance the electronic as well as optical performance due to the increased quantum confinement effect [134].

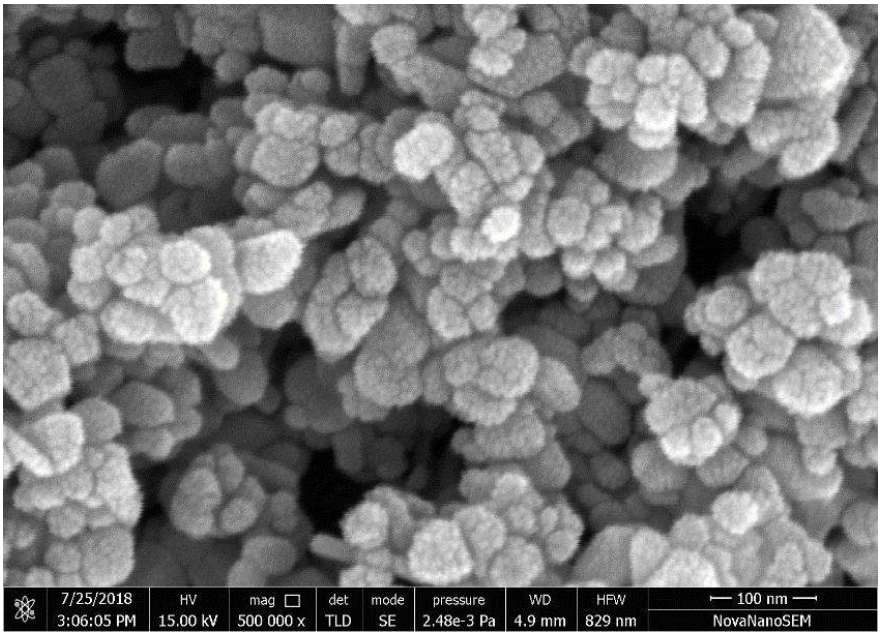

Figure 3.6: HRSEM image of the ZnO nanoparticles on the glass substrate using high-resolution scanning electron microscope (HRSEM, Nova Nano SEM 450, USA).

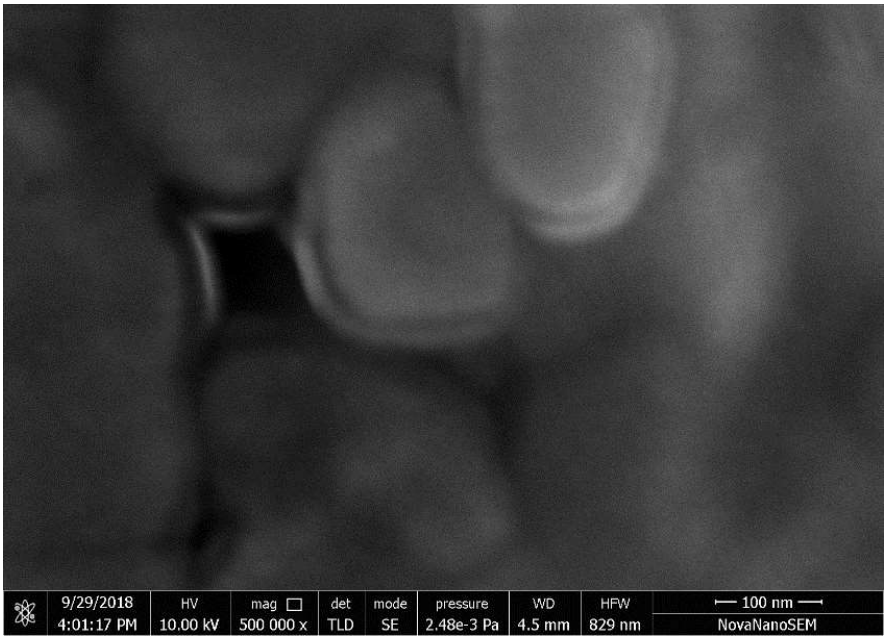

Figure 3.7: HRSEM image of the perovskite $CH_3NH_3PbI_3$ thin film on the glass substrate using high-resolution scanning electron microscope (HRSEM, Nova Nano SEM 450, USA).

.

(c) UV-Vis Analysis

Ultraviolet-Visible (UV-Vis) spectroscopy (V-770 from JASCO, Japan) is used for the optical properties of materials such as reflectance and absorbance. According to Beer

Lambert's equation, absorption coefficient α of sample material is given by following relation [122]:

$$\alpha = 2.303Abs\frac{(\lambda)}{t} \qquad \text{.....(3.1)}$$

where t denotes the thickness of thin film and absorbance coefficient Abs (λ) of a thin film is measured from the absorbance curve, experimentally measured by UV-Visible (UV-Vis) spectroscopy. At room temperature, the measured Abs (λ) of ZnO nanoparticles deposited on the glass substrate, hybrid perovskite $CH_3NH_3PbI_3$ thin film deposited on the glass substrate and perovskite $CH_3NH_3PbI_3$ thin film deposited on ZnO deposited glass substrate are displayed in Figure 3.8.

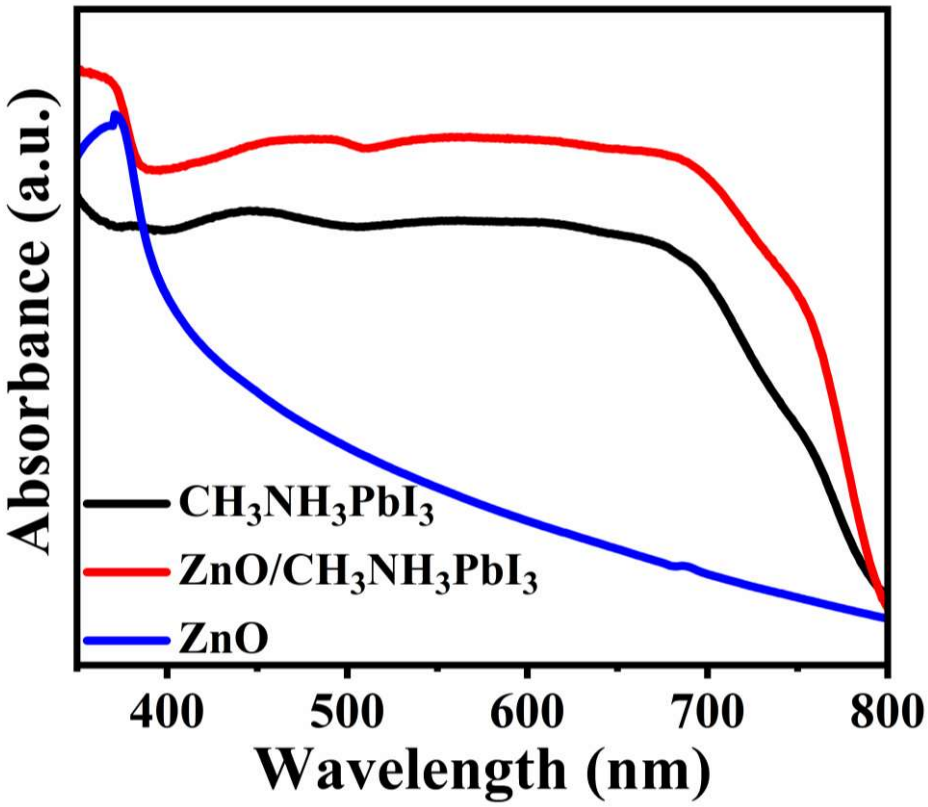

Figure 3.8: Absorbance spectra of the ZnO nanoparticles deposited on the glass substrate, hybrid perovskite $CH_3NH_3PbI_3$ thin film deposited on the glass substrate and perovskite $CH_3NH_3PbI_3$ thin film deposited on ZnO deposited glass substrate using (UV-Vis) spectroscopy (V-770 from JASCO, Japan).

For ZnO NPs thin film, we obtained the maximum absorption in the UV region and strong peak corresponding to 370 nm wavelength and for perovskite $CH_3NH_3PbI_3$ thin film, we obtained a broad spectrum that covered the completely visible spectrum. When perovskite $CH_3NH_3PbI_3$ thin film is deposited on ZnO deposited glass substrate, the absorbance of ZnO/$CH_3NH_3PbI_3$ increased as compared to $CH_3NH_3PbI_3$ thin film which supports further for the appropriateness as wide range visible photodetector using heterostructure [36].

(d) Photoluminescence (PL) Analysis

The photoluminescence (PL) spectroscopy (FLS 980 from Edinburgh instruments, UK) is used to analyze the photoluminescence of ZnO nanoparticles deposited on the glass substrate, hybrid perovskite $CH_3NH_3PbI_3$ thin film deposited on the glass substrate and perovskite $CH_3NH_3PbI_3$ thin film deposited on ZnO deposited glass substrate. The PL emission spectrum of ZnO and $CH_3NH_3PbI_3$ thin film (on glass and ZnO nanoparticles deposited glass substrate) at the excitation wavelength of 370 nm and 405 nm, respectively are shown in Figure 3.9. The emission peaks for ZnO and $CH_3NH_3PbI_3$ thin film are appeared at ~445 nm and ~778 nm, respectively. We have observed a significant reduction in the PL intensity for $CH_3NH_3PbI_3$/ZnO heterostructure. This decrement in the emission intensity or the PL quenching is credited to efficient charge transfer between $CH_3NH_3PbI_3$ and ZnO nanoparticles [135]. The efficient transfer of photogenerated charge carrier enhanced optical absorption. The emission from ZnO nanoparticles may also enhance the absorption in the perovskite film due to additional photo carriers generated in $CH_3NH_3PbI_3$ due to emitted light from ZnO nanoparticles [133]. The enhanced absorption in the perovskite film over ZnO nanoparticles deposited glass substrate was shown in Figure 3.8.

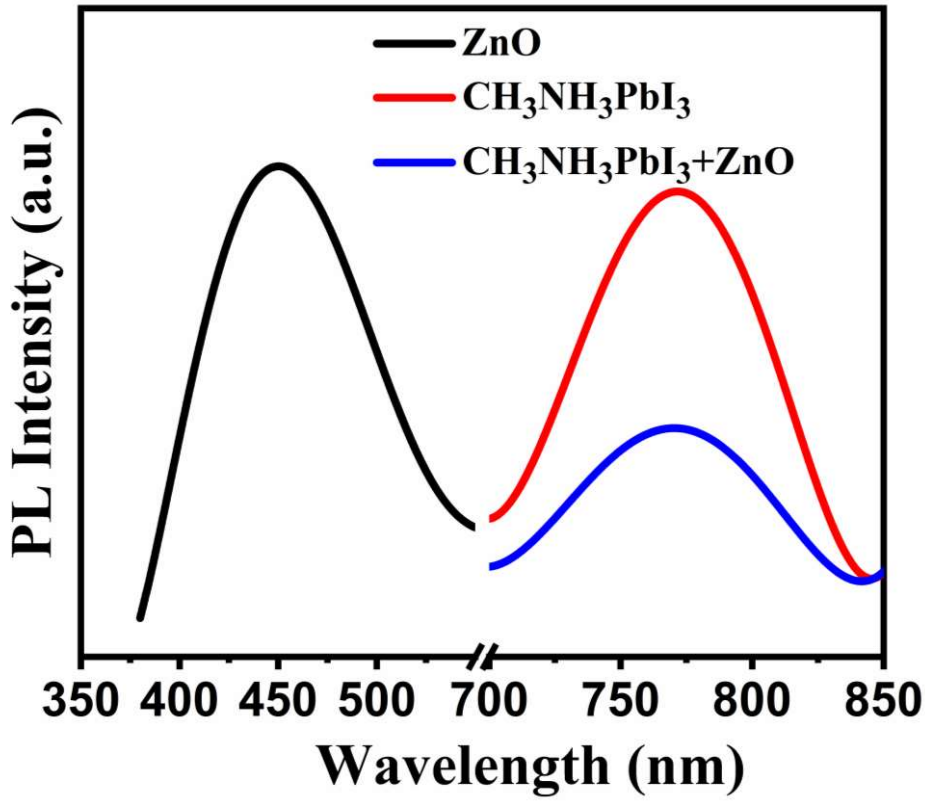

Figure 3.9: Emission spectrum of the ZnO nanoparticles deposited on the glass substrate, hybrid perovskite $CH_3NH_3PbI_3$ thin film deposited on the glass substrate and perovskite $CH_3NH_3PbI_3$ thin film deposited on ZnO deposited glass substrate using photoluminescence (PL) spectroscopy (FLS 980 from Edinburgh Instruments, UK).

3.3.2 Electrical Characterizations

After investigating the thin film properties, we now examined the room temperature electrical characterization via capacitance-voltage (*C-V*) characteristics and current-voltage *(I–V)* characteristics measurements for the fabricated device.

(a) capacitance-voltage (C-V) characteristics

The room temperature capacitance-voltage (*C-V*) characteristics are obtained at 1 MHz frequency using a semiconductor parameter analyzer (B1500A from Keysight, USA) for FTO/ZnO/$CH_3NH_3PbI_3$/MoOx/Ag device. The CV measurement has been done to include only the depletion layer capacitance by avoiding the excess capacitance due to interface states at low frequencies [50], [123]. Capacitance-voltage *C-V* characteristics of

the fabricated heterostructure device is shown in Figure 3.10. The existence of a capacitance confirms the formation of a depletion region at the junction of the heterojunctions device. Negative capacitance due to the different series resistance and interface states at different frequencies [124], [125].

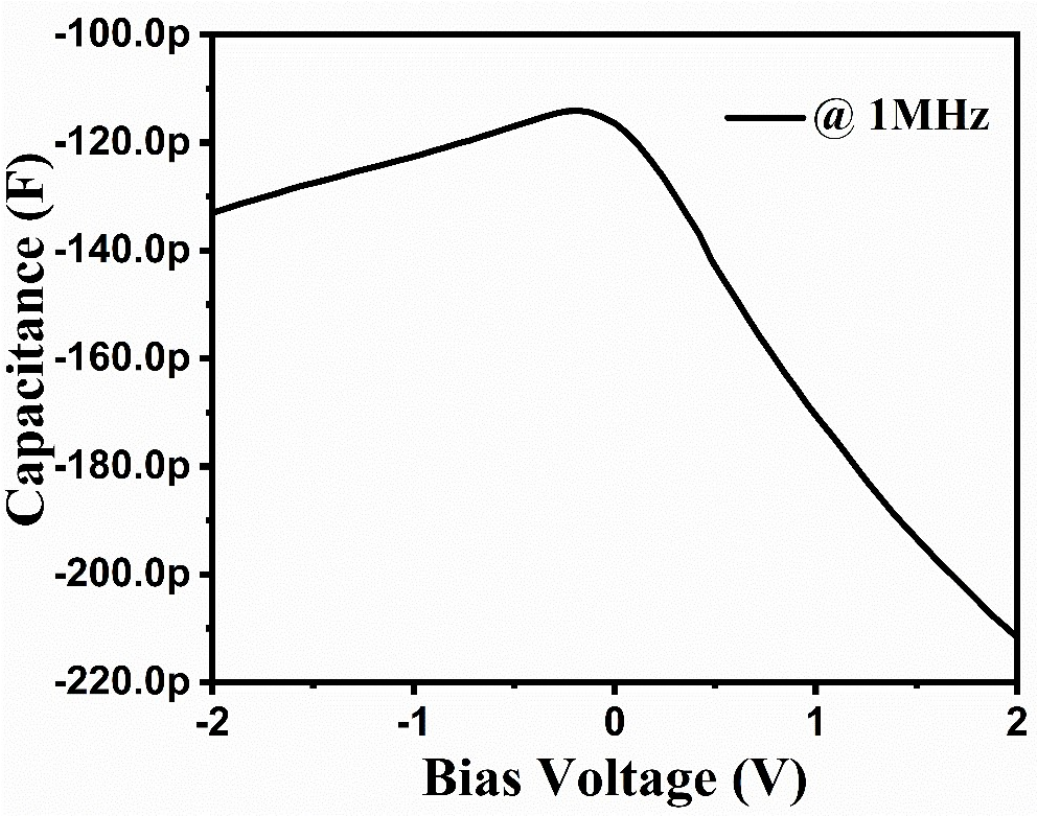

Figure 3.10: Capacitance voltage *(C-V)* characteristics of the fabricated heterostructure device at 1 MHz frequency using a semiconductor parameter analyzer (B1500A from Keysight, USA).

(b) Energy Band Diagram

Now we discussed the photodetection mechanism for fabricated photodetector devices. Note that the operation of the FTO/ZnO/$CH_3NH_3PbI_3$/MoOx/Ag heterojunction device under light illumination involves three steps:

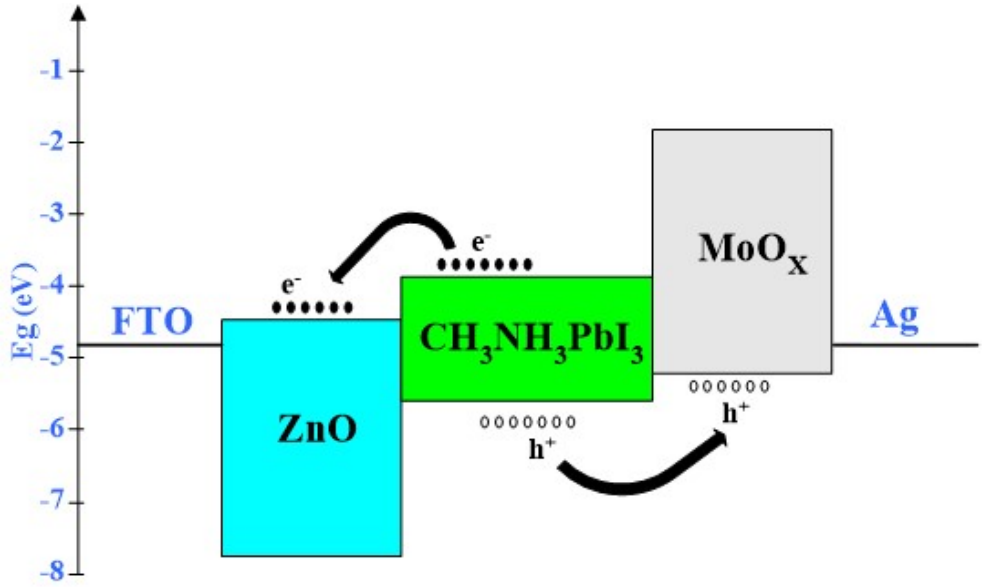

Figure 3.11: Schematic energy band diagram of the proposed heterojunction photodetector.

(i) The generation of charge carrier by incident light.

(ii) The separation and transport of charge carrier by internal field in the depletion region.

(iii) Extraction of charge carrier as terminal current to provide output signal [50], [126].

The operation of the FTO/ZnO/$CH_3NH_3PbI_3$/MoOx/Ag heterojunction photodetector under consideration has been demonstrated in Figure 3.11 through an energy band diagram of a fabricated device under light illumination and reverse bias operation. The fabricated photodetector device is illuminated from (Glass/FTO Side) to gain 100% illumination area. Note that the major portion of the light will be reflected back to open space from the metal surface if the device is illuminated from the metal contact side. The ZnO thin film layer is used as an electron device layer (ETL) in the device. The excess photogenerated electron-hole pairs (EHPs) in the active region (i.e. depletion region of $CH_3NH_3PbI_3$) are drifted out to the inherent electric field of the depletion region. The photogenerated electron moves toward the ZnO layer while the hole moves towards the Ag electrode. The MoOx layer is used as a hole transport layer (HTL) in the device.

(c) current-voltage (I–V) characteristics

The measured current-voltage *(I–V)* characteristics of the FTO/ZnO/$CH_3NH_3PbI_3$/MoOx/Ag heterojunction have been shown in Figure 3.12. The current-voltage *(I–V)* characteristics are measured at room temperature and in -1 V to 1 V bias voltage range by using a semiconductor parameter analyzer (B1500A from Keysight, USA) under dark and illumination of 1 sun (obtained from solar simulator manufactured by PET, USA) condition. The maximum photocurrent of -8.01 mA has been obtained which is almost three times larger than the dark current of -2.71 mA under the reverse bias of 1 V. For reverse saturation current calculation, we compare the current-voltage *(ln I–V)* characteristics as shown in Figure 3.13, of a fabricated heterostructure photodetector device. A reverse saturation current of ~9.4 x10^{-6} A is calculated from the standard diode equation in the dark condition [50].

$$I = I_0 \left\{ exp\left(qV / \eta kT\right) - 1 \right\} \qquad \text{..... (3.2)}$$

where q is the electronic charge, η is the ideality factor of the heterojunction, V is the bias voltage, I_0 is the reverse saturation current, and T is the absolute temperature.

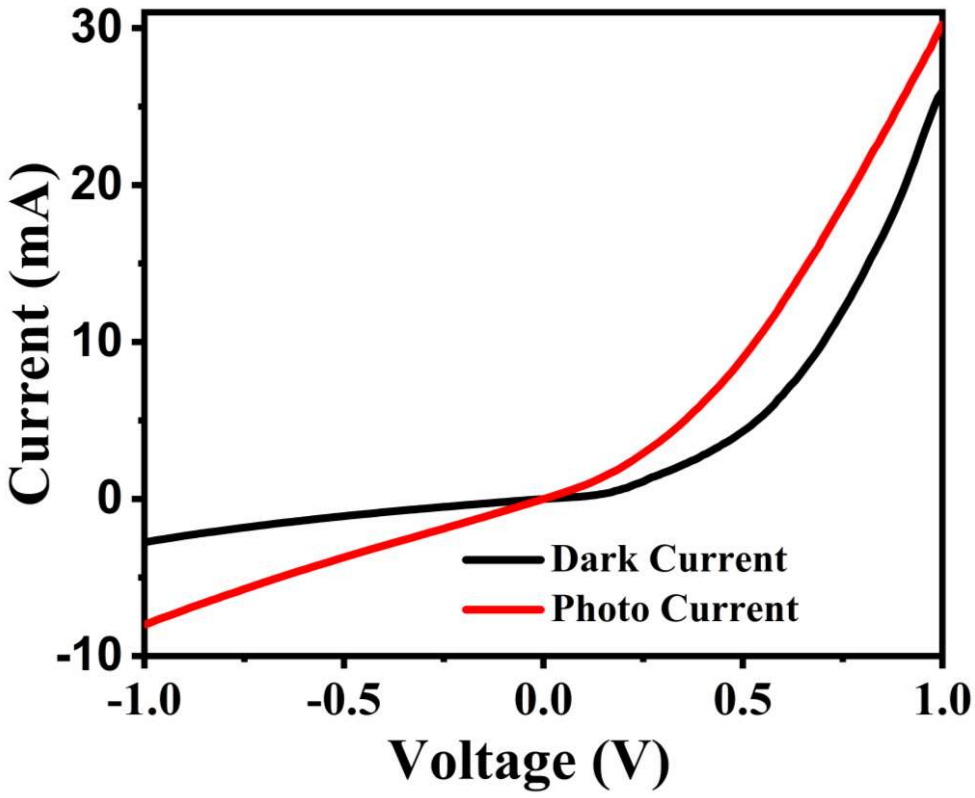

Figure 3.12: Current-voltage (*I-V*) characteristics of the proposed heterojunction photodetector at room temperature and in -1 V to 1 V bias voltage range by using a semiconductor parameter analyzer (B1500A from Keysight, USA) under dark and illumination of 1 sun (obtained from solar simulator manufactured by PET, USA) condition.

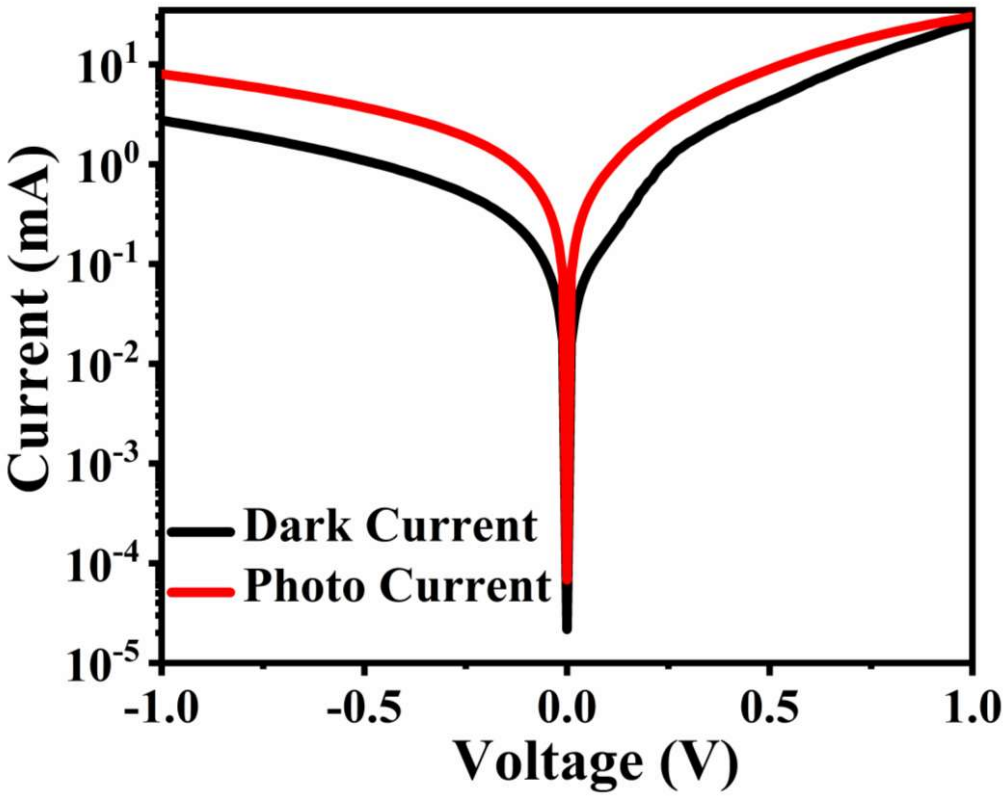

Figure 3.13: Logarithmic current-voltage (*I-V*) characteristics of the proposed heterojunction photodetector at room temperature and in -1 V to 1 V bias voltage range by using a semiconductor parameter analyzer (B1500A from Keysight, USA) under dark and illumination of 1 sun (obtained from solar simulator manufactured by PET, USA) condition.

3.3.3 Optical Characterizations

The important parameter of a photodetector, responsivity (R) is estimated from the wavelength transient characteristics of the heterostructure device in the wide wavelength range obtained from a monochromator (SP2150i from Princeton Instruments, USA) along with a halogen light source. The wavelength (λ) dependent optical power density P_{opt} (λ) of the incident monochromatic light is measured by a power meter (PM100D, Thorlabs). Figure 3.14 shows the responsivity (R) of the proposed photodetector measured over 350 to 700 nm obtained from a monochromator (SP2150i from Princeton Instruments, USA) along with a halogen light source.

The responsivity characteristic shown in Figure 3.14 is calculated using Equation:

$$R(\lambda) = I(\lambda, V)/AP_{opt}(\lambda) \quad \text{..... (3.3)}$$

where I_{light} and I_{dark} represent the current under light and dark conditions, respectively. P_{opt} (λ) and A represent optical power density and the effective exposed area of the heterostructure, respectively. Here, the effective area is 0.0314 cm^2 and the optical power density is ~190 $\mu W/cm^2$ measured by a power meter (PM100D, Thorlabs). The highest responsivity of ~21.8 A/W is obtained near the blue light (~436 nm) at an applied bias voltage of -1V, which is also evident from absorption spectra was shown in Figure 3.8. With the help of the responsivity of the proposed photodetector we can easily calculate the external quantum efficiency (EQE) of the proposed photodetector by using the following relation:

$$EQE(\%) = 1240\frac{R(\lambda)}{\lambda} * 100 \quad \text{..... (3.4)}$$

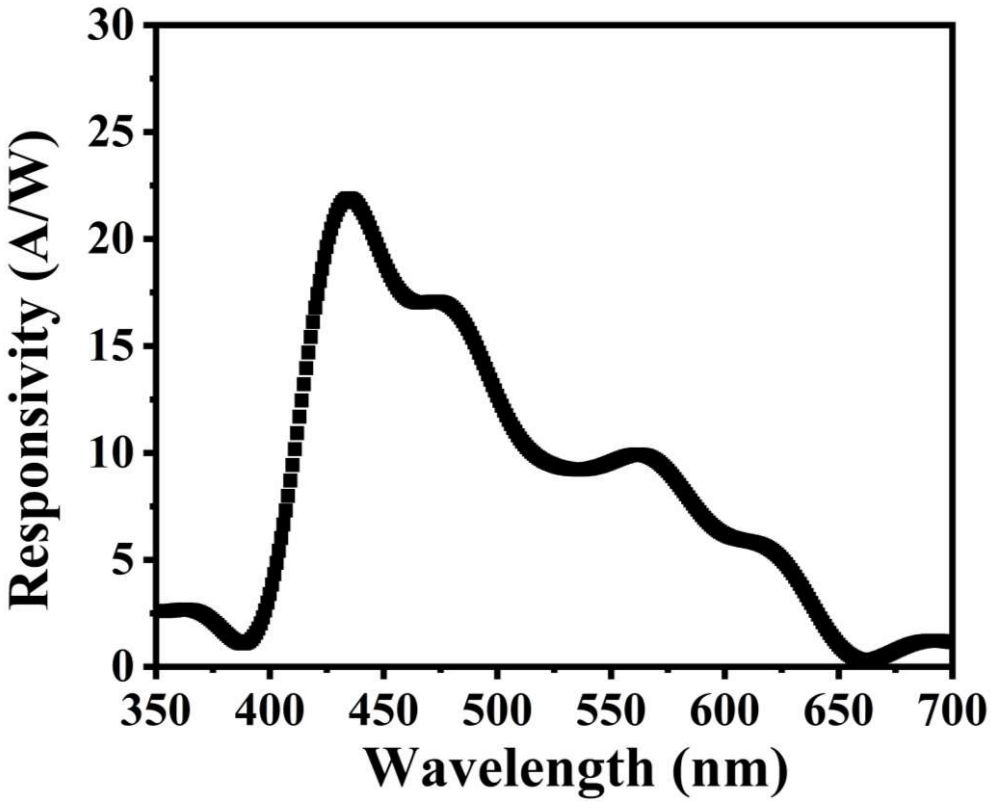

Figure 3.14: Responsivity of the proposed photodetector device against wavelength in the range of 350-700 nm from a monochromator (SP2150i from Princeton Instruments, USA) along with a halogen light source.

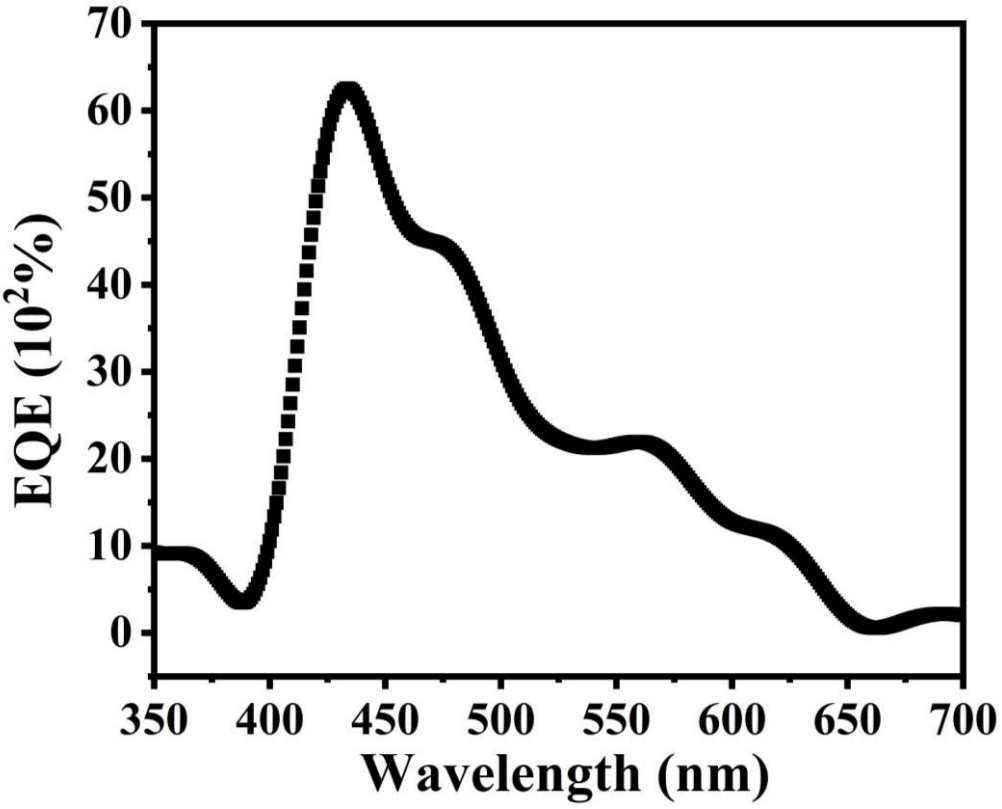

Figure 3.15: External quantum efficiency (EQE) of the proposed photodetector device against wavelength in the range of 350-700 nm from a monochromator (SP2150i from Princeton Instruments, USA) along with a halogen light source.

The maximum value of ~6200% external quantum efficiency (EQE) of the proposed photodetector is obtained at a wavelength of ~436 nm at an applied bias voltage of -1V. Figure 3.15 shows the external quantum efficiency (EQE) of the proposed photodetector measured over 350 to 700 nm.

3.4 Conclusion

In this chapter, nanostructured metal oxide ZnO and hybrid perovskite $CH_3NH_3PbI_3$ thin film are synthesized using the sol-gel chemical route. The structural, morphological, and optical properties are investigated using XRD, HRSEM, UV-Vis, and PL analysis. It is found that the ZnO thin film is crystalline with a hexagonal wurtzite structure and $CH_3NH_3PbI_3$ thin film is crystalline with a tetragonal structure with high phase purity. The heterostructure FTO/ZnO/$CH_3NH_3PbI_3$/MoOx/Ag based photodetector is fabricated

and characterized for optoelectronic properties under dark and illumination of 1 sun as well as monochromatic light. The junction formation in the heterostructure is confirmed by capacitance-voltage *C-V* and current-voltage *I-V* characteristics. The proposed heterojunction device exhibits a maximum value of responsivity ~21.8 A/W and external quantum efficiency (EQE) ~6200% near the blue light spectrum (~436 nm) at an applied bias voltage of -1 V.